Provided for non-commercial research and education use.
Not for reproduction, distribution or commercial use.

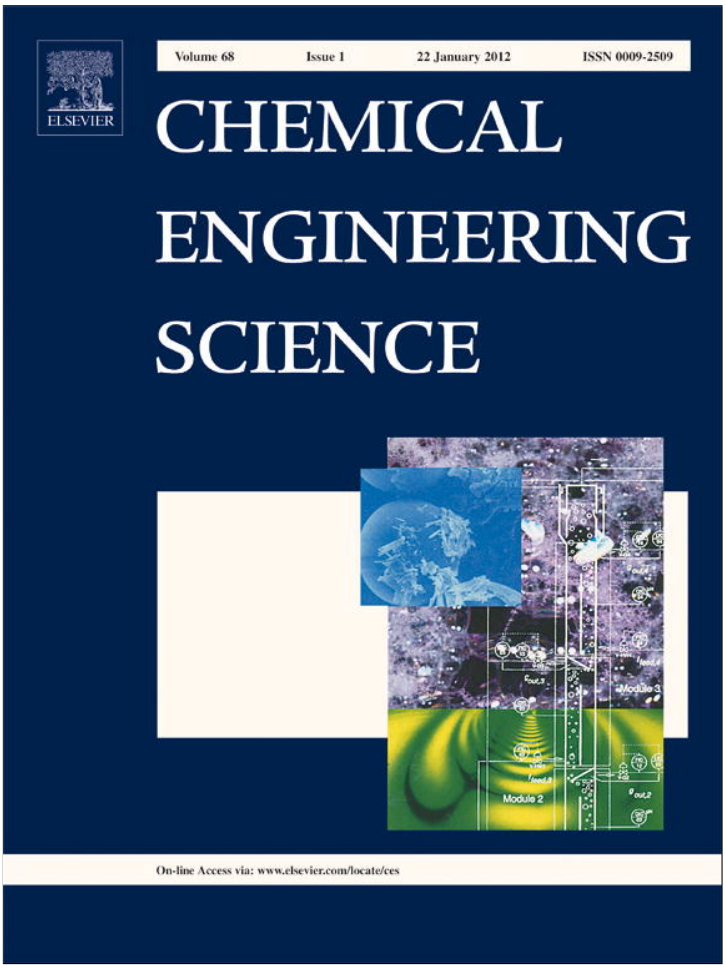

(This is a sample cover image for this issue. The actual cover is not yet available at this time.)

This article appeared in a journal published by Elsevier. The attached copy is furnished to the author for internal non-commercial research and education use, including for instruction at the authors institution and sharing with colleagues.

Other uses, including reproduction and distribution, or selling or licensing copies, or posting to personal, institutional or third party websites are prohibited.

In most cases authors are permitted to post their version of the article (e.g. in Word or Tex form) to their personal website or institutional repository. Authors requiring further information regarding Elsevier's archiving and manuscript policies are encouraged to visit:

http://www.elsevier.com/copyright

Author's personal copy

Chemical Engineering Science 75 (2012) 106–119

Contents lists available at SciVerse ScienceDirect

Chemical Engineering Science

journal homepage: www.elsevier.com/locate/ces

Lattice Boltzmann simulations of pinched flow fractionation

Orest Shardt [a,*], Sushanta K. Mitra [b], J.J. Derksen [a]

[a] Department of Chemical and Materials Engineering, University of Alberta, Edmonton, Alberta, Canada
[b] Department of Mechanical Engineering, University of Alberta, Edmonton, Alberta, Canada

ARTICLE INFO

Article history:
Received 22 September 2011
Received in revised form
8 March 2012
Accepted 13 March 2012
Available online 19 March 2012

Keywords:
Simulation
Laminar flow
Microfluidics
Pinched flow fractionation
Separations
Fluid mechanics

ABSTRACT

Direct numerical simulations of microsphere motion through a microfluidic separation device (pinched flow fractionation, PFF, device) were performed using the lattice Boltzmann method. The results were compared with the original experimental work on PFF by Yamada et al. (2004). The effects of the pinched segment width and the ratio between the particle solution and diluent flow rates were studied. Both analyses showed agreement with the experimental trends. Previous modelling of PFF has relied on the assumption that particles follow streamlines, and this assumption was evaluated. The simulations indicated that large particles experience a lift force due to a region of low pressure between the particle and the wall of the pinch. The lift force attracts the particles to the wall as they exit the pinched segment. Smaller particles experience a much weaker force. This force may provide an explanation for the experimental observation that a sharp expansion provides better separation performance than a gradual expansion, an effect that cannot be explained by streamline analyses.

© 2012 Elsevier Ltd. All rights reserved.

1. Introduction

The motion of solid particles is important in a wide variety of microfluidic devices. In many of these devices, geometric constraints, internal hydrodynamic forces, or external forces are used to control the motion of the particles. Often the goal is to separate the particles by size. The design of such devices requires models for the interactions between the particles and the flow to account for effects such as the lift on particles in shear flow and drag due to Dean flow (Berger et al., 1983). Modelling and simulation are complicated by the fact that next to viscous effects, inertial effects may be important at the moderate Reynolds numbers that can be achieved in microfluidic devices, implying that the simplifying assumption of creeping flow is not applicable. The challenges in understanding the behaviour of particles in microfluidic systems are emphasized by a recent study of microsphere motion in which the assumption that the centre of mass of a particle has the same speed as the particle-free flow was shown to become inaccurate as the width of a microchannel approaches the diameter of the spheres (Di Carlo et al., 2009). Thus, confinement, in addition to finite particle size and mass, causes particle velocities to deviate from the velocity of the undisturbed fluid. Computational studies with fully resolved hydrodynamics and coupled particle motion are a valuable tool for studying complex microfluidic systems when the validity of simplifying assumptions is poor or uncertain. In this work, we present lattice Boltzmann simulations of a device for separating particles by size.

Pinched flow fractionation (PFF), a method for the continuous separation of particles by size, was proposed by Yamada et al. (2004). In PFF, particles with different sizes in a fluid stream are pushed against one wall of a narrow channel, the pinch, by the flow of an injected diluent. Due to their alignment along that wall, the centres of mass of the particles follow different streamlines. When the particles enter a wider channel, they separate as the streamlines spread. The method has been used to separate 15 and 30 μm poly(styrene/divinylbenzene) beads in a viscous aqueous Dextran solution (Yamada et al., 2004), erythrocytes from blood plasma (Takagi et al., 2005), and the droplets of an emulsion (Maenaka et al., 2008). In the latter two examples, the irregular shape and deformability of the dispersed phase introduce additional complexity to performance analyses. Enhanced PFF methods have been proposed (Lee et al., 2011b; Vig and Kristensen, 2008). We study rigid spherical particles in simple PFF.

The analysis and prediction of PFF performance have been primarily based on the assumptions that particles follow the streamlines of the particle-free flow and do not disturb the flow (Jain and Posner, 2008; Vig and Kristensen, 2008; Yamada et al., 2004). The first empirical model for PFF was a linear amplification relationship that was determined from the paths of fluorescent microsphere tracers (1.0 μm diameter) (Yamada et al., 2004)

$$y_o = \left(w_p - \frac{D}{2}\right)\frac{w_o}{w_p} \tag{1}$$

* Corresponding author.
E-mail addresses: shardt@ualberta.ca (O. Shardt), sushanta.mitra@ualberta.ca (S.K. Mitra), jos@ualberta.ca (J.J. Derksen).

0009-2509/$ - see front matter © 2012 Elsevier Ltd. All rights reserved.
http://dx.doi.org/10.1016/j.ces.2012.03.013

Author's personal copy

where w_o is the width of the outlet, w_p is the width of the pinch, y_o is the position of the particle centre at the outlet, and D is the diameter of the particle. This model assumes that particles reach the upper wall while in the pinched segment. If the particles do not reach the upper wall, linear amplification implies that

$$\frac{y_o}{y_p} = \frac{w_o}{w_p} \tag{2}$$

where y_p is the position of the particle centre when it is in the pinched segment. This empirical model assumes that the streamlines, as determined from the tracer trajectories, exhibit linear amplification and that the microspheres being separated follow these streamlines. Mortensen (2007) points out that for low Reynolds number (Stokes) flow, the assumption that particles follow streamlines cannot explain some experimentally-observed phenomena. For example, if particles follow streamlines, then separation performance should be independent of the geometry between the pinch and outlet because the positions of the streamlines in the outlet depend only on the final width of the channel. Yamada et al., however, observed better performance with a sudden expansion (step, 180° boundary angle) than with a gradual expansion (linear, 60° angle). Mortensen indicates a need for more detailed modelling of PFF to better understand and design PFF devices.

Vig (2010) provides a review of recent improvements to the empirical linear model proposed by Yamada et al. (2004). The model of Andersen et al. (2009) employs the analytical solution for the laminar flow profile in a rectangular channel and shows better agreement with experimental results. While this model provides an improvement to the linear streamline amplification model, which is accurate in the limit of high aspect ratio channels, it still relies on the assumption that particles follow streamlines. Vig and Kristensen (2008) and Vig (2010) modelled PFF by assuming that particles follow streamlines, but included a corner effect. This corner effect accounts for the geometric constraints that prevent particles from following streamlines that pass closer to a wall than the radius of the particle. Their 2D computational model used the finite element method (FEM) to obtain the streamlines of the flow. It is based on the assumptions that the particles do not disturb the flow and the walls provide only a geometric constraint and cause no forces on the particles. The model is considered semi-3D because a body force that is inversely proportional to the fluid velocity is used to account for the hydraulic drag of the walls in the omitted dimension (the depth of the channel).

To allow better modelling of PFF, the reasons for the deviation of the particles from the streamlines need to be understood. These deviations appear to be caused by the complex hydrodynamics arising from the confinement of the particles in a narrow channel. The purpose of the present work is to use the lattice Boltzmann method to perform direct three-dimensional simulations of PFF. The flow of single spherical particles of two different diameters through a PFF device was simulated. The simulation results were compared with the experimental performance data reported by Yamada et al. (2004). Such simulations with fully resolved hydrodynamics and full resolution of the solid–liquid interface provide a way to determine the limitations of simplifying assumptions and identify which physical effects are essential for modelling particle behaviour. The simulations could therefore be used to guide the development of simpler yet accurate models.

This paper is organized as follows. First, the mathematical modelling of PFF is described, followed by a description of the required numerical methods. These include the lattice Boltzmann method (LBM), its boundary conditions, the immersed boundary method, and the methods for the numerical integration of particle motion. Several validation benchmarks are described before the full simulations of PFF are presented and discussed. Finally, the research is summarized and main conclusions are provided.

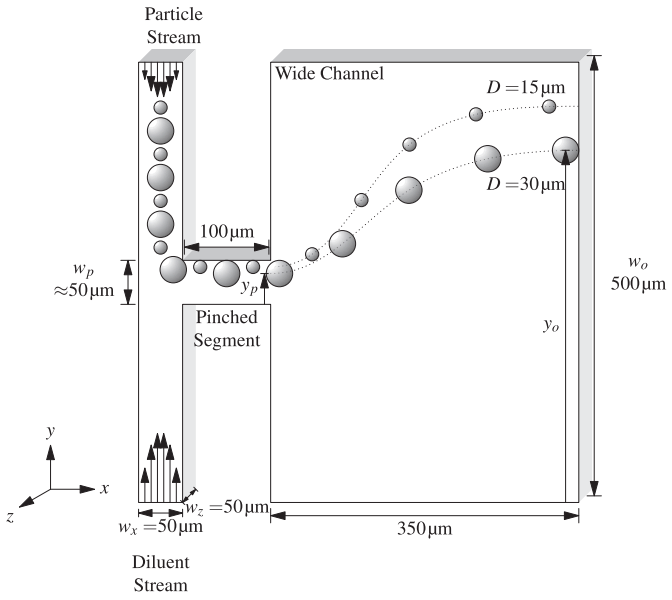

Fig. 1. Schematic of the simulated pinched flow fractionation device.

2. Mathematical modelling and simulation set-up

2.1. Geometry

A schematic of the simulated device geometry is shown in Fig. 1. The geometry employed by Yamada et al. was modified to facilitate the simulations yet allow a comparison between the experiments and simulations to be meaningful. One difference in the geometry is the angle between the inlet channels. While Yamada et al. used an angle of 60°, the simulated geometry has an angle of 180° to simplify the implementation of the boundary conditions on a cubic lattice. This difference in the geometry, though it may affect the position the particles reach in the pinched segment, is considered minor because our main interest is in the behaviour of the particles as they exit the pinched segment. Another difference is the smaller outlet width (500 μm versus 1000 μm). For either width, the ratio between the pinched channel and outlet channel widths is high, and it is expected that the vertical position of particles normalized by the width of the outlet channel would be similar in both cases. The length of the outlet, 350 μm, was chosen to limit simulation time by selecting the shortest length for which FEM simulations with COMSOL (COMSOL AB, 2010) showed a minimal difference in the streamlines when compared with a longer outlet channel.

To allow comparison with the experimental work, the parameters in the simulations were chosen to match the experimental system as closely as possible. In LBM simulations, the distance between lattice nodes Δx is taken to be one, and the time interval Δt of each simulation time step is also one. Quantities used in the simulations, such as length and viscosity, are given in lattice units (l.u.) and the actual units are omitted. For example, a viscosity of 0.1 l.u. means 0.1 $\Delta x^2/\Delta t$. The matching between the simulations and experiments is performed through dimensionless numbers. Based on the ratio of the particle diameter and the pinched segment width, we simulate particles with equivalent physical diameters of 15 and 30 μm, as in the experiments. The particle over fluid density ratio was 1.08. The long computation time imposed by LBM stability constraints prevents running simulations at a Reynolds

Author's personal copy

number that matches the experimental flow rate and fluid viscosity. While Yamada et al. employed a highly viscous Dextran solution to avoid sedimentation of the particles before they entered the PFF device, we overcome numerical constraints by matching with the Reynolds number for water at the same flow rate as the experiments (140 μl/h). As a result of this choice, the simulated Reynolds number is one order of magnitude higher than the experimental Reynolds number. Nevertheless, the simulations can be compared with the experimental results due to the observation that the particle trajectories are Reynolds number independent at the low Reynolds numbers considered (Section 3.6). This Reynolds number independence is supported by the experimental evidence of Yamada et al., who showed a small change in particle positions over the wide range of flow rates from 70 to 560 μl/h that correspond to Reynolds numbers (Re_z as defined later) from 0.01 to 0.1.

2.2. Governing equations

The fluid flowing through the PFF device is assumed to be incompressible and Newtonian. Therefore, the flow can be described using the Navier–Stokes equation

$$\rho_f(\partial_t + \vec{u}\cdot\nabla)\vec{u} = -\nabla P + \mu\nabla^2\vec{u} + \vec{b} \tag{3}$$

where ρ_f is the density of the fluid, $\vec{u}$ is the fluid velocity, P is the pressure, μ is the dynamic viscosity (the kinematic viscosity v is μ/ρ_f), and $\vec{b}$ is the sum of all body forces. Mass conservation implies the continuity equation

$$\nabla\cdot\vec{u} = 0 \tag{4}$$

In the absence of a body force and time-varying boundary conditions, non-dimensionalization of the Navier–Stokes equation provides one dimensionless parameter, the Reynolds number Re, given by

$$Re = \frac{uL}{v} \tag{5}$$

where u is a characteristic speed and L is a characteristic length. Due to the low speeds and small sizes encountered in microfluidic devices, the flow is typically laminar, and this is the case for the device and parameter range being simulated. The lattice Boltzmann method is used to simulate the flow of a fluid governed by these equations, as described in Section 2.3.

The motion of particles is governed by Newton's laws of motion. The forces acting on the particles are determined from the immersed boundary method for imposing a no-slip condition on the surface of a moving interface, as described in Section 2.4.2. Though the polystyrene particles being simulated are slightly more dense than the simulated fluid (water), gravity is neglected due to the low density ratio and short time span during which the particles pass through the PFF device. This is justified by the Stokes law terminal Reynolds number for a settling 30 μm polystyrene sphere, which is at least two orders of magnitude smaller than the Reynolds number for the translational velocity. The translational motion of the particles is governed by (Derksen and Sundaresan, 2007)

$$\frac{\mathrm{d}\vec{x}_p}{\mathrm{d}t} = \vec{u}_p \tag{6}$$

$$(\rho_s-\rho_f)\frac{\pi}{6}D^3\frac{\mathrm{d}\vec{u}_p}{\mathrm{d}t} = \vec{F}_{LBM} \tag{7}$$

where $\vec{x}_p$ is the position of the particle centre of mass, $\vec{u}_p$ is the velocity of the particle centre of mass, D is the diameter of the spherical particle, ρ_s is the density of the solid particle ($\rho_s/\rho_f = 1.08$ for the polystyrene beads used by Yamada et al., 2004, in water), and $\vec{F}_{LBM}$ is the force on the particle determined from the immersed boundary method.

The rotational motion is governed by (Derksen and Sundaresan, 2007; and Shardt and Derksen, 2011)

$$\frac{\mathrm{d}q}{\mathrm{d}t} = \frac{1}{2}q\circ(0,\vec{\omega}_p) \tag{8}$$

$$(\rho_s-\rho_f)\frac{\pi}{60}D^5\frac{\mathrm{d}\vec{\omega}_p}{\mathrm{d}t} = \vec{S}^{-1}\vec{T}_{LBM} \tag{9}$$

where q is the unit quaternion describing the orientation of the particle, $\vec{\omega}_p$ is the angular velocity of the sphere with respect to a body-fixed reference frame, "$\circ$" denotes quaternion multiplication, $\vec{T}_{LBM}$ is the torque on the particle (in the laboratory reference frame) due to the forces from the immersed boundary method, and $\vec{S}$ is the transformation matrix for conversion from body-fixed to laboratory coordinates. Eq. (8) describes the change in orientation due to rotation; Eq. (9) describes the change in rotation rate due to the applied torque. The numerical solution of the equations governing the translational and rotational motion of a spherical particle is described in Section 2.5.

2.3. Lattice Boltzmann method

The lattice Boltzmann method is used as the flow solver. This method simulates the evolution of the velocity distribution of the molecules in a fluid, which is governed by the Boltzmann equation. With the correct choice of equilibrium distribution and lattice symmetry, the lattice Boltzmann method simulates the Navier–Stokes equations (Aidun and Clausen, 2010; Chen and Doolen, 1998). The macroscopic hydrodynamic variables are obtained as the moments of the velocity probability distribution f. For example, the density and fluid momentum (and thus velocity) are given by

$$\rho = \sum_i f_i \tag{10}$$

$$\rho\vec{u} = \sum_i f_i\vec{c}_i \tag{11}$$

where f_i is proportional to the probability of a fluid molecule moving with velocity $\vec{c}_i$. In the present work, the BGK-like LBM proposed by Eggels and Somers is used (Eggels and Somers, 1995; Somers, 1993). One of its benefits is stability over a broad range of viscosities (Derksen and Sundaresan, 2007). This method employs 18 discrete velocities $\vec{c}_i$ (with a corresponding set of 18 weighting factors w_i) in a regular cubic lattice.

To simulate incompressible flow, the Mach number $\|\vec{u}\|/c_s$ must be kept low, where $c_s \sim O(1)$ is the speed of sound in the LBM. Therefore, the parameters for the simulations were chosen to ensure that the maximum fluid velocity was approximately 0.01 l.u.

2.4. Boundary conditions

2.4.1. Inlets, outlet, and walls

Lattice Boltzmann simulations involve two steps: streaming, in which probability densities are propagated to adjacent nodes, and collision, in which the velocity distribution at each node relaxes to the local equilibrium. During the streaming step, the densities entering each node are required. In the bulk fluid, they are obtained from the adjacent nodes. At a boundary of the fluid domain, the incoming densities are unknown, and must be specified by imposing a boundary condition. For a boundary with a fixed velocity $\vec{u}$, Eggels and Somers (1995) provide the

Author's personal copy

condition

$$f_i - f_{-i} = \frac{w_i \rho}{6} \vec{c}_i \cdot \vec{u} \tag{12}$$

where the subscript $-i$ means the index j such that $\vec{c}_j = -\vec{c}_i$. This is a relationship between the known densities leaving across the boundary in direction $\vec{c}_i$ and the unknown densities entering the domain in direction $\vec{c}_{-i}$. To reduce entrance effects at the inlets that would occur if a flat profile were imposed, an approximation to the solution for steady laminar flow in a square channel was used

$$v(x,z) = \frac{16 v_{peak}}{w_x^2 w_z^2} x(w_x - x) z(w_z - z) \tag{13}$$

where v_{peak} is the maximum velocity of the profile, w_x is the width (x-direction) of the channel, w_z is the depth (z-direction), and $v(x,z)$ is the non-zero component (y component) of the inlet velocity $\vec{u}$. The use of this approximate solution is computationally faster than evaluation of the exact solution for laminar flow. The no-slip boundary condition, which is applied on all walls, is a special case of the fixed velocity condition with $\vec{u} = 0$:

$$f_{-i} = f_i \tag{14}$$

This is called the bounceback condition because the density entering in the direction $\vec{c}_{-i}$ is the same as the density leaving in the direction $\vec{c}_i$.

The outlet requires special treatment because the pressure and flow profile at the outlet are not known a priori. Furthermore, for simulations with many time steps, such as those in the present work, conservation of mass is essential. Assuming a linear pressure gradient at the outlet, the incoming f_i at the outlet at position (x,y,z) are taken to be

$$f_i(x,y,z) = \alpha f_i(x-1,y,z) \tag{15}$$

where the constant α is determined such that the densities leaving and entering at the outlet and both inlets are exactly balanced. This ensures mass conservation to within machine precision. This boundary condition provides accurate results, as detailed in Appendix A.

2.4.2. Immersed boundary method

The immersed boundary method allows the relatively easy enforcement of a no-slip boundary condition on a moving surface. In this method, the surface of each particle is specified as a collection of surface points, the interior of the particles contains fluid, and body forces are applied to the fluid nodes adjacent to the interface. These body forces counteract any slip between the solid particle surface and the fluid, forcing the velocity of the fluid to match the velocity of the translating and rotating surface, thus ensuring that the no-slip condition is satisfied. The particular immersed boundary method employed in the present work is based on Goldstein et al. (1993). A more detailed description of the method that was used can be found in Derksen and Sundaresan (2007) and ten Cate (2002). One important detail is that a viscosity-dependent calibration is required to accurately simulate spheres with a particular size (Ladd, 1994). Based on the previous work on sedimentation, a particle hydrodynamic diameter of 12 l.u. was chosen to ensure sufficient resolution of the interface and flow. Consequently, uniformly distributed surface points for spheres with hydrodynamic diameters of 12 l.u. were obtained for viscosities of 0.1 and 0.2 l.u. The calibration is based on the drag on an infinite cubic lattice of spheres (Sangani and Acrivos, 1982).

2.5. Particle motion

The integration of the equations governing particle motion was performed using finite difference approximations. The details are provided in Shardt and Derksen (2011). The particle position, governed by Eq. (6), was updated using explicit Euler integration. The quaternion equation, Eq. (8), was updated using second order Runge–Kutta integration with renormalization of the quaternion at every time step. Explicit Euler integration of Eqs. (7) and (9) is unstable at low density ratios. Therefore, the improved-accuracy split-derivative method described by Shardt and Derksen (2011) was used for the integration of the translational and angular velocities.

Collisions with the walls were modelled as fully elastic, frictionless collisions: If after the position update the particle was found to be intersecting a wall (i.e. the distance between the particle centre and wall was less than the particle radius), then the velocity component pointing towards the wall was reversed, and the particle was moved away from the wall by the same distance it had penetrated the wall. This simulates an elastic rebound upon collision.

2.6. Implementation

Custom Fortran code based on previous sedimentation research was used (Derksen and Sundaresan, 2007; Shardt and Derksen, 2011). Parallelization with OpenMP was used to reduce execution time. The fluid domain was initialized with a density of $\rho_f = 8$ and no flow. It was found that a steady flow field was achieved within 6000 time steps without a particle. The immersed boundary and particle motion integration code were then enabled, and the particle motion and fluid flow were simulated until the particle reached the end of the outlet channel. The motion of the particle from its initial position in the middle of the inlet channel to the outlet took about 400,000 time steps, depending on the path taken by the particle.

2.7. Simulation set-up

The conditions for the 16 simulations that were used to study PFF are listed in Table 1. The first 10 simulations examine the effect of changing the ratio between the particle solution and diluent flow rates. The flow ratios are the same as those used by Yamada et al. (2004). The last six simulations examine the effect

Table 1
Parameters for the simulations.

Run	Domain size, $nx \times ny \times nz$	Viscosity, v (l.u.)	Particle diameter, D/w_z	Flow ratio, particle:diluent	Pinch width, w_p/w_z
1	$400 \times 400 \times 41$	0.2286	0.29	1:6	0.98
2	$400 \times 400 \times 41$	0.2286	0.29	9:19	0.98
3	$400 \times 400 \times 41$	0.2286	0.29	1:1	0.98
4	$400 \times 400 \times 41$	0.2286	0.29	19:9	0.98
5	$400 \times 400 \times 41$	0.2286	0.29	6:1	0.98
6	$200 \times 200 \times 21$	0.1143	0.57	1:6	0.95
7	$200 \times 200 \times 21$	0.1143	0.57	9:19	0.95
8	$200 \times 200 \times 21$	0.1143	0.57	1:1	0.95
9	$200 \times 200 \times 21$	0.1143	0.57	19:9	0.95
10	$200 \times 200 \times 21$	0.1143	0.57	6:1	0.95
11	$400 \times 400 \times 41$	0.2286	0.29	1:6	0.88
12	$400 \times 400 \times 41$	0.2286	0.29	1:6	1.07
13	$400 \times 400 \times 41$	0.2286	0.29	1:6	1.66
14	$200 \times 200 \times 21$	0.1143	0.57	1:6	0.86
15	$200 \times 200 \times 21$	0.1143	0.57	1:6	1.05
16	$200 \times 200 \times 21$	0.1143	0.57	1:6	1.62

Author's personal copy

of the pinch segment width at a constant flow ratio. To reduce the computational time required to simulate particles of two different sizes, the particle size was kept constant at the minimum needed to ensure adequate resolution, 12 l.u., and the domain size was reduced by a factor of two to simulate the flow of particles with twice the diameter. To ensure Reynolds number similarity while keeping the maximum velocity at 0.01 l.u. with both resolutions, the kinematic viscosity was scaled by a factor of two.

3. Results and discussion

3.1. Validation

The simulated velocity profile in the centre of the pinched segment for Run 13 is compared in Fig. 2 with the analytical solution for laminar flow in a rectangular channel (van der Graaf et al., 2006)

$$u(y,z) = u_0\left[1-\left(\frac{z}{c}\right)^2 + 4\sum_{k=1}^{\infty}\frac{(-1)^k}{\alpha_k^3}\frac{\cosh\left(\frac{\alpha_k y}{c}\right)}{\cosh\left(\frac{\alpha_k b}{c}\right)}\cos\left(\frac{\alpha_k z}{c}\right)\right] \tag{16}$$

where the rectangular domain is $-b \le y \le b$ and $-c \le z \le c$, $\alpha_k = (2k-1)\pi/2$, and $u_0 = ((2c)^2/8\mu)(\partial P/\partial x)$. Good agreement can be seen. In fact, relative errors are below 1% away from the edges, about 5% within one node of the edges, and about 10% for the corner nodes. The equivalent physical flow rates through the pinch were 143.3 and 146.5 μl/h in the high resolution and low resolution runs, respectively. They are within 2% of each other and match the experimental flow rate of 140 μl/h. Using the channel depth ($w_z = 50$ μm) as the characteristic length and the average velocity through the pinch as the characteristic velocity, the Reynolds number Re_z for the simulations is 0.8. Considering that the 10 wt% Dextran solution used by Yamada et al. is about 30 times more viscous than water (both the kinematic and dynamic viscosity assuming a small difference between the solution density and the density of water, see e.g. Akashi et al., 2000), the experimental channel Reynolds number was about 0.03. Inertial effects can therefore be expected to be greater in the simulations than in the experiments of Yamada et al. (2004).

The grid independence of the particle-free flow was verified by comparing the streamlines for the large (nx=400) and small (nx=200) simulations in the xy-plane through the middle of the domain. The last saved flow cross-sections at the end of the initialization period were used. At this time, the flow had reached steady state. Every pair of runs was compared. The results for Runs 1 and 6 are shown in Fig. 3 and are typical of all eight pairs. The streamlines are almost identical showing that the correct scaling has been used and the grid is sufficiently fine to correctly resolve the particle-free flow.

Fig. 4 shows the initial and final vertical positions of 10 streamlines starting in the middle of the pinched segment and ending at the outlet. As for Fig. 3, the streamlines were obtained for the particle-free flow before the sphere was added to the simulation. The vertical positions have been normalized by the width of the channel at their respective positions. Points for the particle-free flow of every run are shown and are nearly indistinguishable. It can be seen that streamlines spread nearly linearly; these results are consistent with the linear amplification observed experimentally by Yamada et al. (2004) using fluorescent microspheres. However, the streamlines end slightly farther from the centre than a linear relationship would predict. The deviation may be due to the inaccuracy of the linear amplification assumption as considered by Jain and Posner (2008) and Andersen et al. (2009) or the reduced length of the outlet channel in the simulations.

The immersed boundary and particle motion aspects of the simulations have been validated in previous work. For example, the methods have been used to simulate wave instabilities in dense suspensions (Derksen and Sundaresan, 2007), drag on agglomerates of spheres near walls (Derksen and Larsen, 2011), and particle-induced mixing in microfluidic devices (Derksen, 2009). The sedimentation of dense suspensions of non-spherical

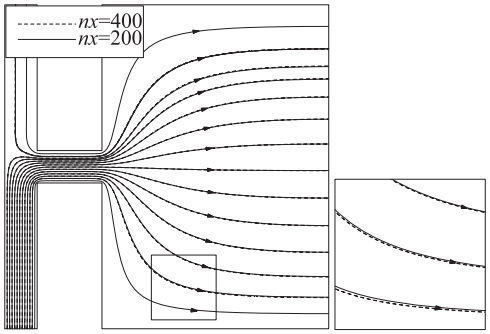

Fig. 3. Comparison of the streamlines for Runs 1 (nx=400) and 6 (nx=200) showing the similarity of the flow fields.

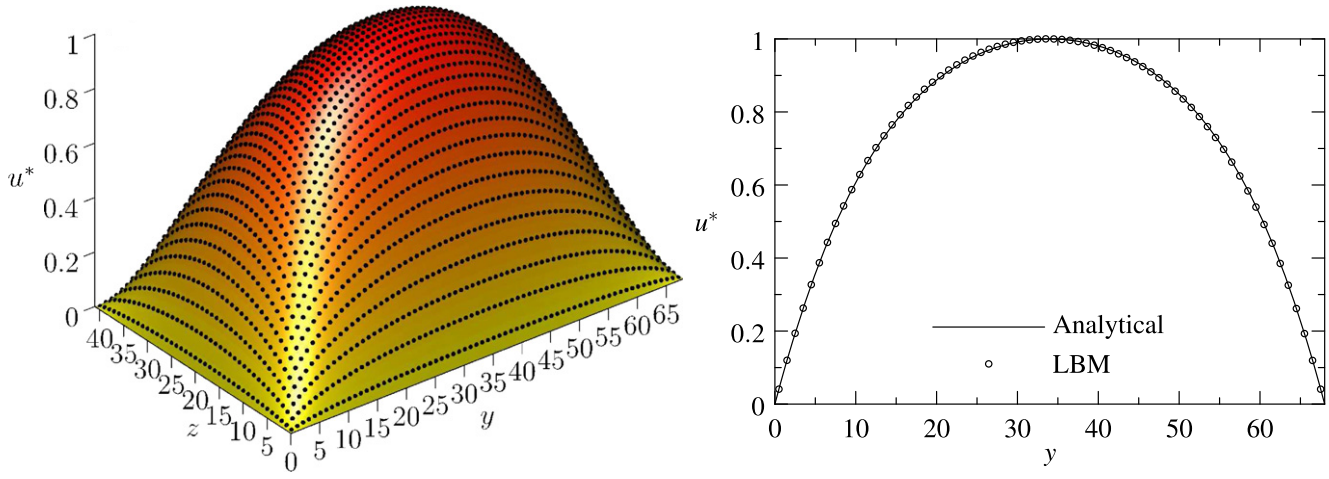

Fig. 2. Comparison of the velocity profile ($u^* = u/u_{max}$) in the centre of the pinched segment for Run 13 (dots) with the analytical solution (surface, left). The velocity at z=20 is shown on the right.

Author's personal copy

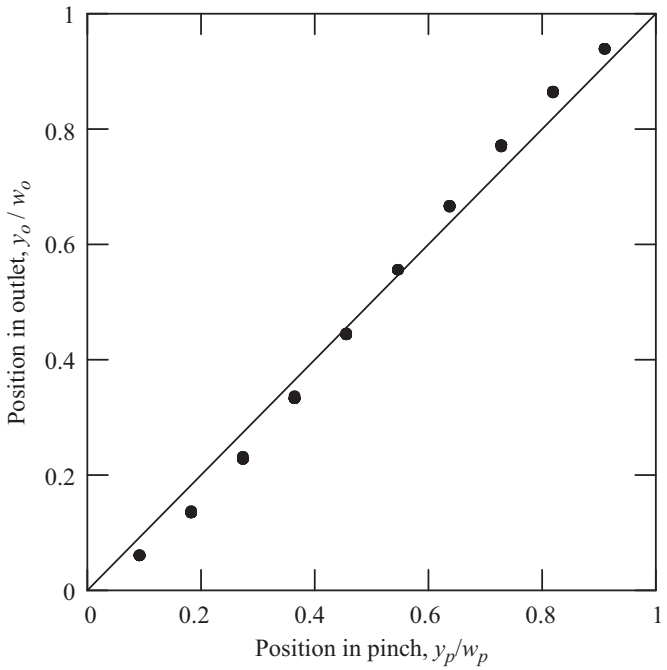

Fig. 4. Initial and final vertical positions of 10 streamlines of the particle-free flow starting in the middle of the pinched segment and ending at the outlet. The line shows the prediction of the linear amplification model (Eq. (2)), and the dots show the simulation results for the 10 streamlines and 16 runs. The dots for different runs are indistinguishable.

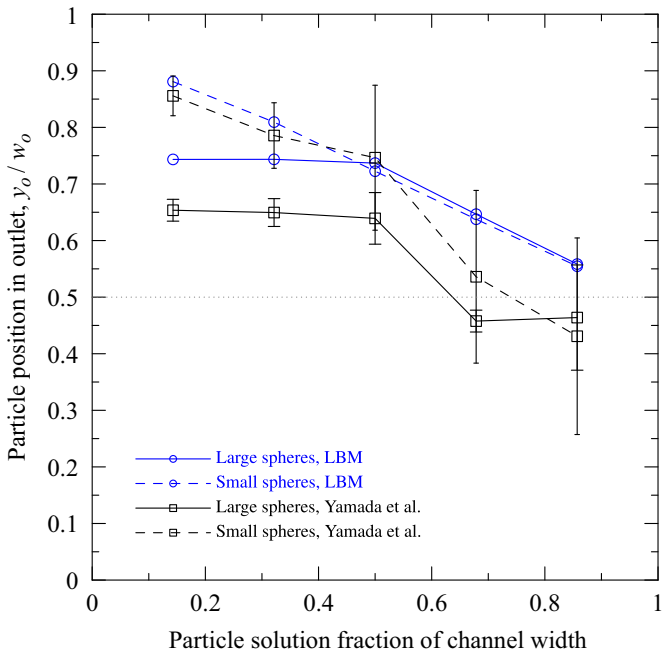

Fig. 5. Comparison of the simulated flow ratio effect with the experimental results obtained by Yamada et al. (2004).

particles (rigid red blood cells) at low density ratios has also been simulated using these methods (Shardt and Derksen, 2011). Based on these previous studies, a particle diameter of 12 l.u. was chosen to ensure adequate resolution for accurate results.

3.2. Computing resources

We now turn our attention to the simulations of pinched flow fractionation. The computational workload for these simulations was split between several nodes on a cluster and a desktop computer. Each of the simulations with a small particle was performed using two CPUs on one node of a Westgrid cluster. Runtimes ranged from 328 to 506 h (14.7–21.1 days). The variation in the runtime is primarily due to the fact that the particles reach the outlet in fewer time steps if they follow a faster or shorter streamline. The large particle simulations were run on a desktop computer with an Intel Core i5 750 CPU, and all runs were completed in less than one week (168 h). Each high resolution simulation required 1129 MB of memory; the low resolution simulations required about 140 MB each.

3.3. Effect of flow ratio

The simulation data for the first 10 runs allow the effect of the flow ratio on the position of the particles at the outlet to be analysed. Fig. 5 provides a comparison of the simulation results with the experimental data of Yamada et al. (2004). As described previously (Section 2.1), the simulation results and the experimental results can be compared despite the difference in Reynolds number. At low Reynolds numbers, the path of the particles appears to be independent of the Reynolds number, as discussed in Section 3.6. It should be noted that we compare simulations of a single particle starting in the middle of the inlet channel with average positions from experiments with uncontrolled initial positions. The average position from the particles in the inlet might not have been the middle of the channel. Comparing simulations of one particle with the experimental suspensions is acceptable because of the low experimental solids volume fraction ($< 0.1\%$). The "particle solution fraction of the channel width" (Yamada et al., 2004) is the fraction of the pinched segment occupied by the fluid that entered with the particles. It is given by $Q_p/(Q_p+Q_d)$, where Q_p is the particle stream flow rate and Q_d is the diluent stream flow rate. In both the experimental results and simulations, the large particle position reaches a maximum at about the same flow ratio while the position of the small particles varies throughout the range of flow ratios. One unusual feature of the experimental results is that the large particles reach a position below the centre of the outlet when the diluent flow rate is low. In the limit of no diluent flow, one would expect the particles to end on average in the middle of the outlet channel. With diluent flow, the mean position should be above the middle. Reasons for the offset in the large particle position are uncertain, but there is general agreement in the trend of the particle position as a function of the flow ratio. The large range of the experimental small particle positions also makes comparison of the simulated and experimental trends difficult. Agreement can be seen in terms of the downward trend, though the slope differs and the discrepancy increases at lower diluent flow rates where the range of the experimental observations is wider.

Fig. 6 compares the positions of particles with the predictions of the empirical linear amplification model. The performance of the device in terms of the difference between the positions of the large and small particles is also shown. As expected, better separation performance is achieved as the diluent flow rate is increased. Both large and small particles deviate from the linear amplification assumption; the deviation of the large particles is greater and increases with increasing diluent flow rate. One interesting feature of the simulations is the reversal of the relative positions of the small and large particles at low diluent flow rates (i.e. large particles end higher in the outlet than the small particles). As will be discussed later, this may be due to the interaction of the large particles with the walls of the pinched segment. Considering the ranges of the small particle positions

Author's personal copy

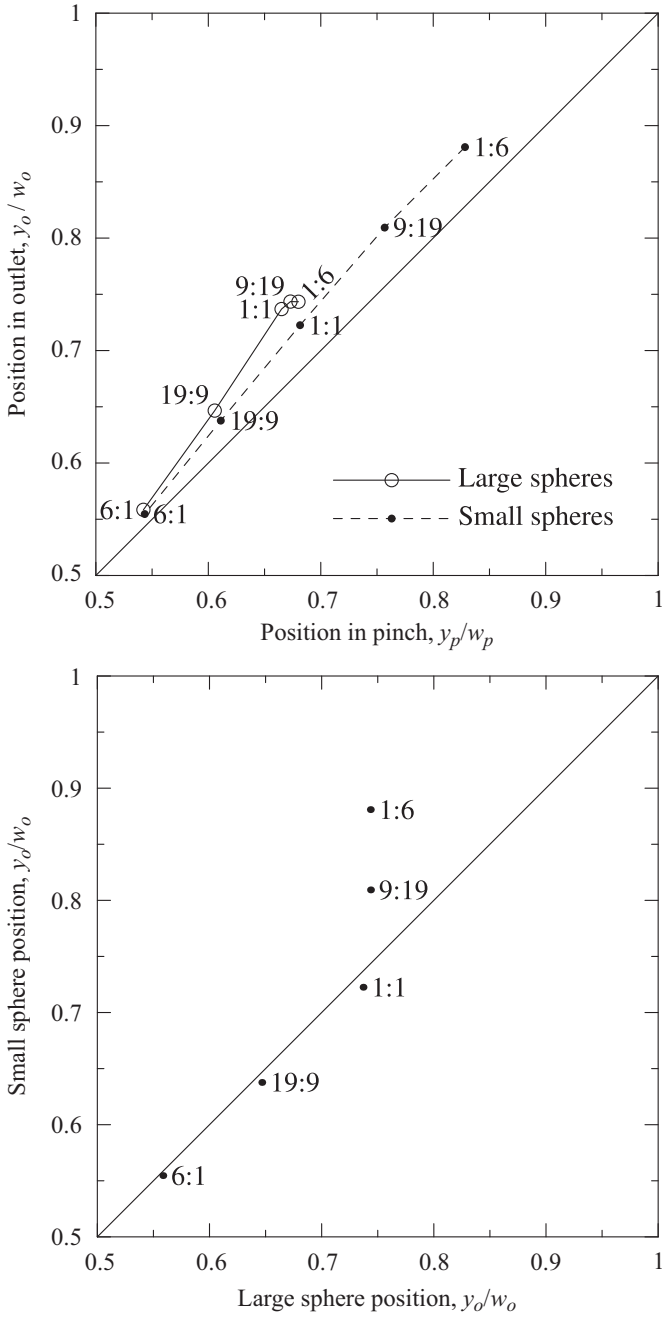

Fig. 6. Separation performance (bottom) and comparison of particle positions with the linear amplification model (Eq. (2), top) with different flow ratios. The labels show the ratio of the particle stream flow rate to diluent flow rate.

observed by Yamada et al., it is not possible to validate this phenomenon using their experimental data.

3.4. Effect of pinched segment width

The simulated and experimental particle positions at the outlet are compared in nondimensional form in Table 2. Nearly the same pinch widths were considered as those used by Yamada et al.: 45, 55, and 85 μm in the simulations versus 47, 56, and 82 μm in the experimental work. The particle:diluent flow ratio was 1:6 as in the experimental work. Excellent agreement can be seen between the simulations and experiments. It should be noted, however, that the simulation results are for a single particle while the experimental values are averaged over many

Table 2
Effect of the pinched segment width on the position of the particles at a flow ratio of 1:6.

Pinch width w_p (μm)		Small sphere position y_o/w_o		Large sphere position y_o/w_o	
Experimental	LBM	Experimental	LBM	Experimental	LBM
47	45	0.87 ± 0.01	0.868	0.66 ± 0.01	0.711
56	55	0.89 ± 0.02	0.891	0.76 ± 0.02	0.769
82	85	0.89 ± 0.03	0.897	0.81 ± 0.02	0.850

particles with potentially different initial positions. It is evident that the position of the small spheres remains nearly constant while the large spheres move higher as the pinch becomes wider.

The changes in particle position in response to changes in the width of the pinched segment are shown in Fig. 7. These figures include the data for Runs 1 and 6 which had a 50 μm wide pinch and the same flow ratio as the other runs shown. It can be seen that the position of the small particles is nearly independent of the pinched segment width. This is consistent with the assumption that particles follow streamlines: the particles should reach the same position independent of the geometry between the initial and final position (Mortensen, 2007). Unlike the small particles, the large particles reach different positions depending on the width of the pinched segment. As the width decreases, the deviation from linear amplification increases. This suggests that the particles interact with the upper wall while in the pinch, and the strength of the interaction increases as the width decreases. Overall, the results are intuitive: a narrower pinch affects the large particles more than the small particles and enhances separation performance.

3.5. Particle rotation and cross-streamline migration

In all the simulations, the spheres reached a higher position at the outlet than streamlines would predict. To examine this phenomenon in greater detail, the trajectories of the particles were compared with streamlines passing through the position of the particle at the start of the simulation and upon reaching the middle of the pinched segment. Sample comparisons of the particle trajectories with the streamlines are shown in Fig. 8 for the runs with varying flow ratios and in Fig. 9 for the runs with varying pinched segment widths. The streamlines were obtained for the *xy*-plane through the middle of the simulated domain. Due to the geometric constraints where the inlet reaches the pinched segment, the large particles quickly deviate from the initial streamline after colliding with the wall. After entering the pinched segment, the extent of the deviation from the streamline through the particle position in the pinch depends on the particle size, flow ratio, and pinched segment width. The figures reiterate the previous observations regarding the position of the particles in the outlet and in the pinch: the particles reach the outlet at a higher position than the streamline through the position of the particle in the pinch would predict. Large particles deviate more from the streamline than the small particles. The closer a particle is to the upper wall, which occurs with higher diluent flow rates and narrower pinches, the more it deviates from the streamlines.

One feature of the particle motion not considered by streamline analyses is the rotation of the particles into, through, and out of the pinched segment. Figs. 10 and 11 show the angular velocity of the particles about the *z*-axis as they travel through the PFF device. The use of the segment width in the nondimensionalization of the angular velocity was chosen for comparison with the experimental work of Di Carlo et al. (2009). The particles do not rotate until they begin entering the pinched segment. Through

Author's personal copy

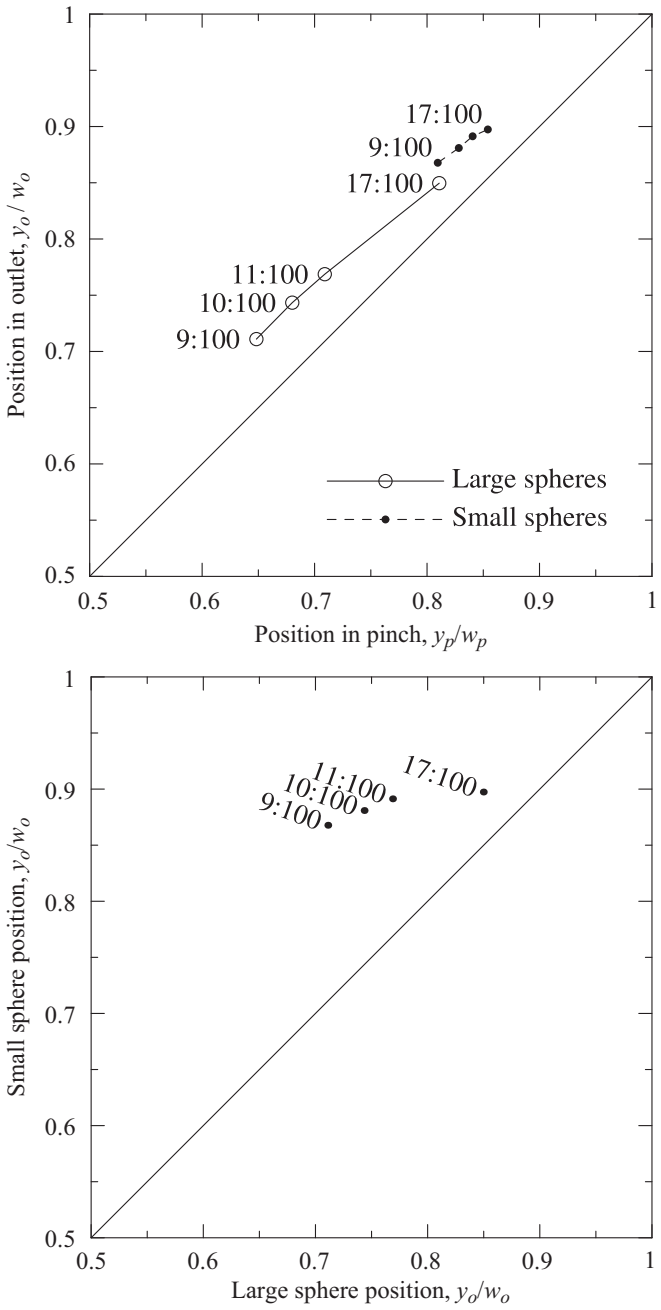

Fig. 7. Separation performance (bottom) and comparison of particle positions with the linear amplification model (Eq. (2), top) with different pinched segment widths. The labels show $w_p : w_o$.

the pinched segment, the angular velocity is constant until it increases as the particle exits the pinch. The angular velocity then decays rapidly in the outlet channel. At the channel Reynolds number of 20 for which Di Carlo et al. report rotation rates (compared with 0.8 in the present simulations), smaller particles at their equilibrium positions rotate faster than larger particles. In the simulations, the nondimensional angular velocity is higher for the smaller particles when the particles are nearer to the wall (i.e. when the diluent flow rate is high or the pinch is narrow). While the experimental nondimensional angular velocities at a Reynolds number of 20 vary between 0.13 and 0.5, the angular velocities through the pinched segment vary between about 0.1 and 1.2 in the simulations. Possible reasons for the differences are the Reynolds number and the comparison of angular velocities at the equilibrium position (experimental) and non-equilibrium position (simulations). In the simulations, the angular velocity depends strongly on the flow ratio and pinch width. Wall and particle surface roughness in the experimental system (both are assumed smooth in the simulations) or insufficient resolution in the simulations may also play a role. Lubrication forces were not added to the simulations to compensate for low resolutions in the narrow gaps between the spheres and channel walls.

To quantify the deviation of the particles from the streamlines of the undisturbed flow, the component of the particle velocity perpendicular to the velocity of the undisturbed flow was computed. The perpendicular relative velocity component $u_\perp$ normalized by the particle speed $\|\vec{u}_p\|$ is shown in Fig. 12 for the runs with varying flow ratios and in Fig. 13 for the runs with varying pinched segment widths. A positive velocity is towards the upper wall of the pinch and the inner left and right walls adjacent to the upper wall of the pinch. In general, the particles deviate from the streamlines when they enter and leave the pinched segment. Spikes in the perpendicular velocity occur when the particle collides with the wall and the direction is reversed to handle the collision. In general, it can be seen that the large particles move faster from the streamlines. The perpendicular velocity component increases with increasing diluent flow rate and decreasing pinched segment width. Thus, the closer a particle is to the upper wall, the faster it moves away from the streamline. Vig (2010) considered the geometric constraints that prevent particles from following streamlines, and the model handles the changes in position due to contact with the wall, but does not include the attraction to the wall when the particle leaves the pinched segment. The motion towards the wall causes the particles to follow a path that is closer to the wall than a streamline through the position of the particle when it is in the pinch.

To determine the origin of the lift force that causes the deviation from the streamlines, the pressure fields around the particle were analyzed for Run 7. Fig. 14 shows the pressure field in the *xy*-plane around the particle while it is rotating and translating past the middle of the pinched segment. The angular velocity of the particle is such that all points on the particle are moving in the positive *x*-direction, i.e. the angular velocity is less than the velocity for perfect rolling along the upper wall. The pressure has been normalized with respect to the pressure drop between the diluent inlet (with pressure P_i) and the outlet (with pressure P_o). A high pressure region is evident in the gap between the particle and the wall in the portion downstream of the particle. A low pressure region exists in the portion of the gap that is upstream of the particle. The shape of the pressure field is due to the rotation and translation of the particle which cause fluid to be drawn into the gap (relative to the bulk flow farther from the particle) in the downstream portion and pushed from the gap in the upstream portion.

The pressure fields around the particle as it enters the wider outlet segment are shown in Fig. 15. Fig. 16 shows a sample velocity field cross-section. A low pressure region can be seen between the particle and the upper corner. This low pressure region is likely the cause of the attraction towards the upper wall experienced primarily by the large particles as they leave the pinched segment. The low pressure region and the consequent lift force may explain why Yamada et al. observed that a sharp expansion provides better separation performance than a gradual expansion. With a gradual expansion, the particle would be close to the wall for a longer time. Attraction to the wall would move the particle to a higher streamline in the outlet channel, thereby worsening separation performance. Attraction to the wall may also explain why large particles could reach a higher position in the outlet than small particles when the diluent flow rate is low.

Author's personal copy

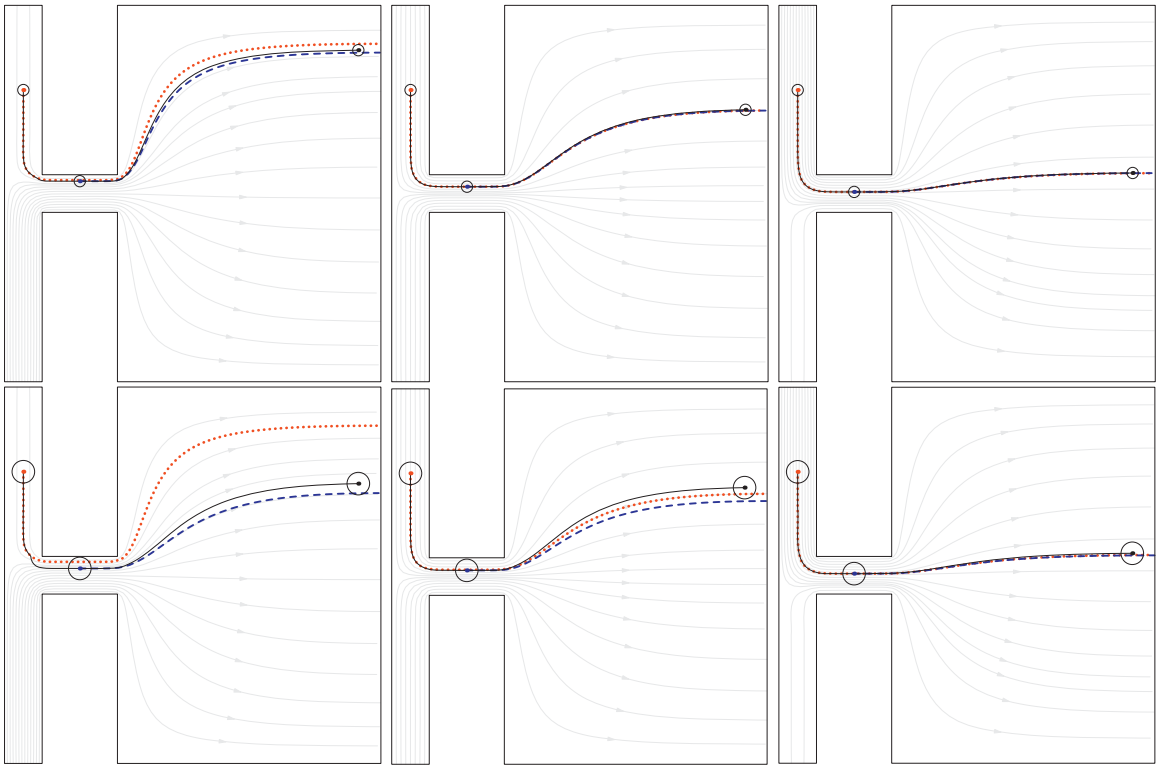

Fig. 8. Comparison of the small (top) and large (bottom) particle trajectories (black) with a streamline through the initial particle position (dotted red) and through the particle position in the centre of the pinched segment (dashed blue) for the runs with varying flow ratios: Runs 1 and 6 (left), 3 and 8 (middle), and 5 and 10 (right). (For interpretation of the references to color in this figure legend, the reader is referred to the web version of this article.)

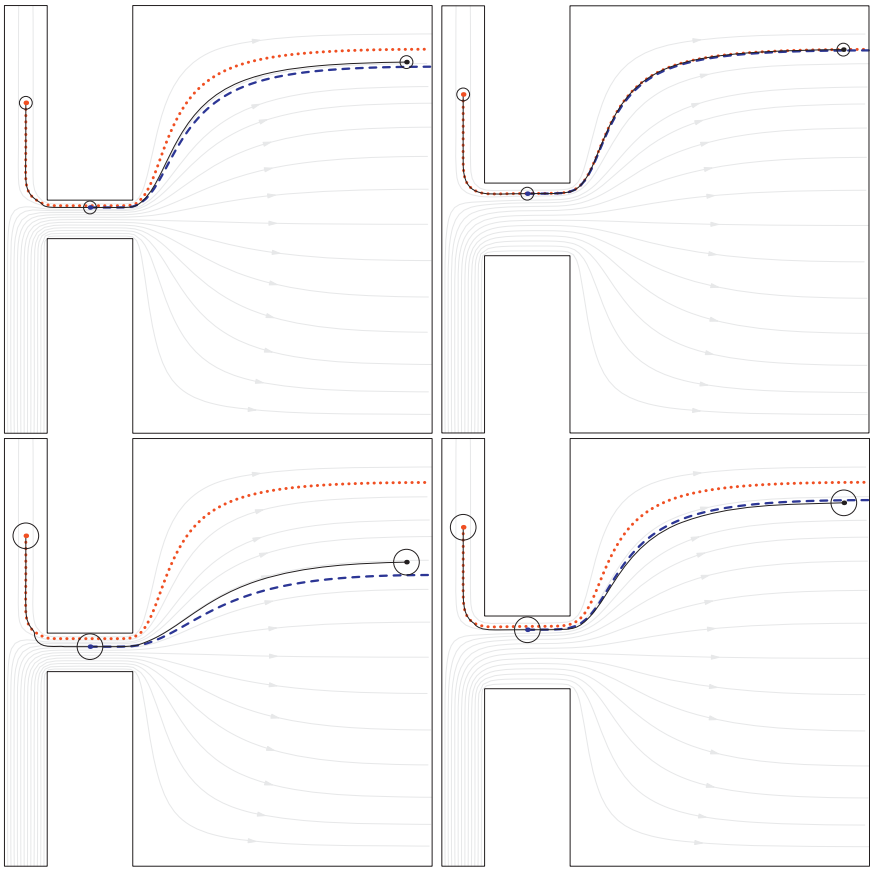

Fig. 9. Comparison of the small (top) and large (bottom) particle trajectories (black) with a streamline through the initial particle position (dotted red) and through the particle position in the centre of the pinched segment (dashed blue) for the runs with varying pinch widths: Runs 11 and 14 (left), and 13 and 16 (right). (For interpretation of the references to color in this figure legend, the reader is referred to the web version of this article.)

Author's personal copy

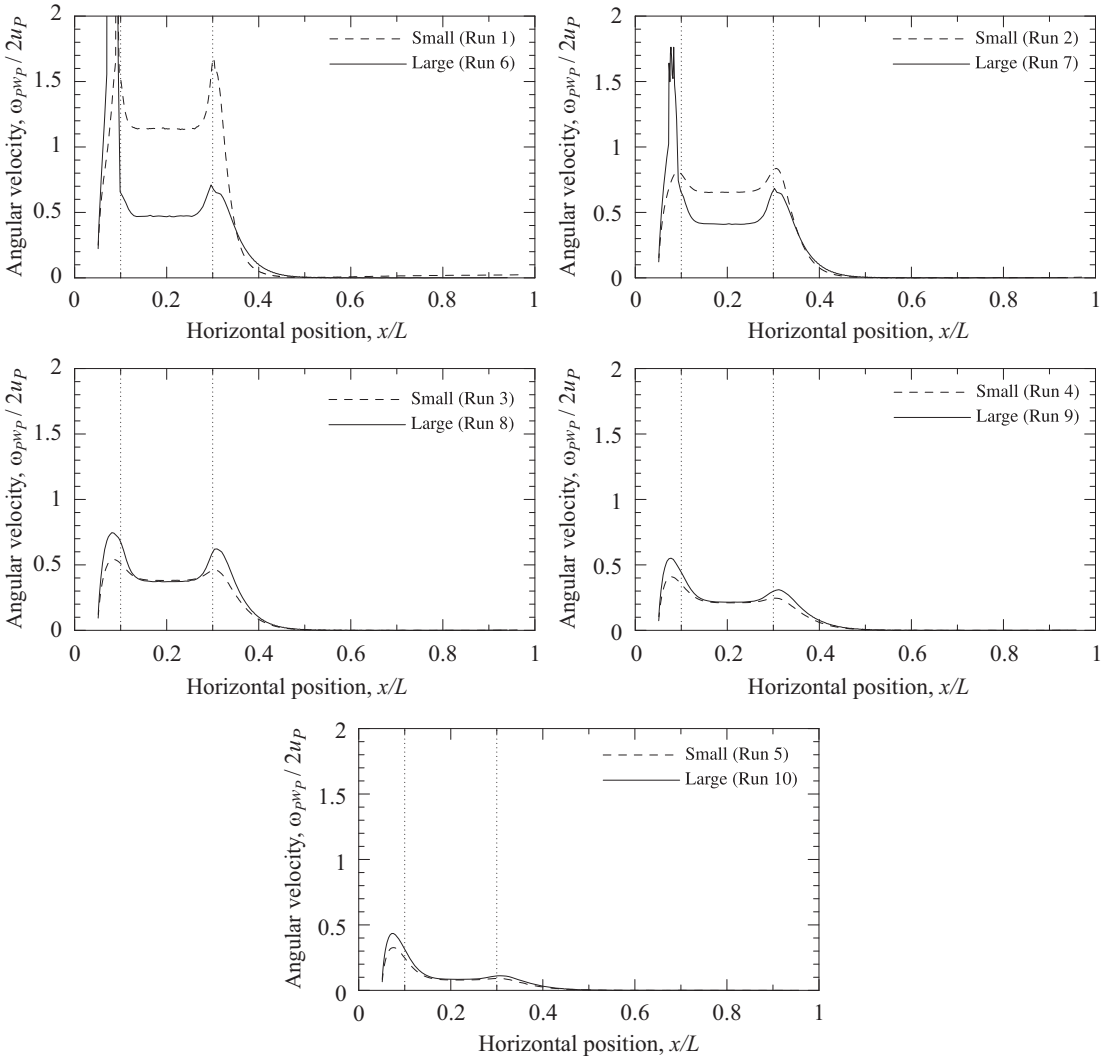

Fig. 10. Angular velocity of the sphere for the runs with varying flow ratios. The vertical lines indicate the start and end of the pinched segment.

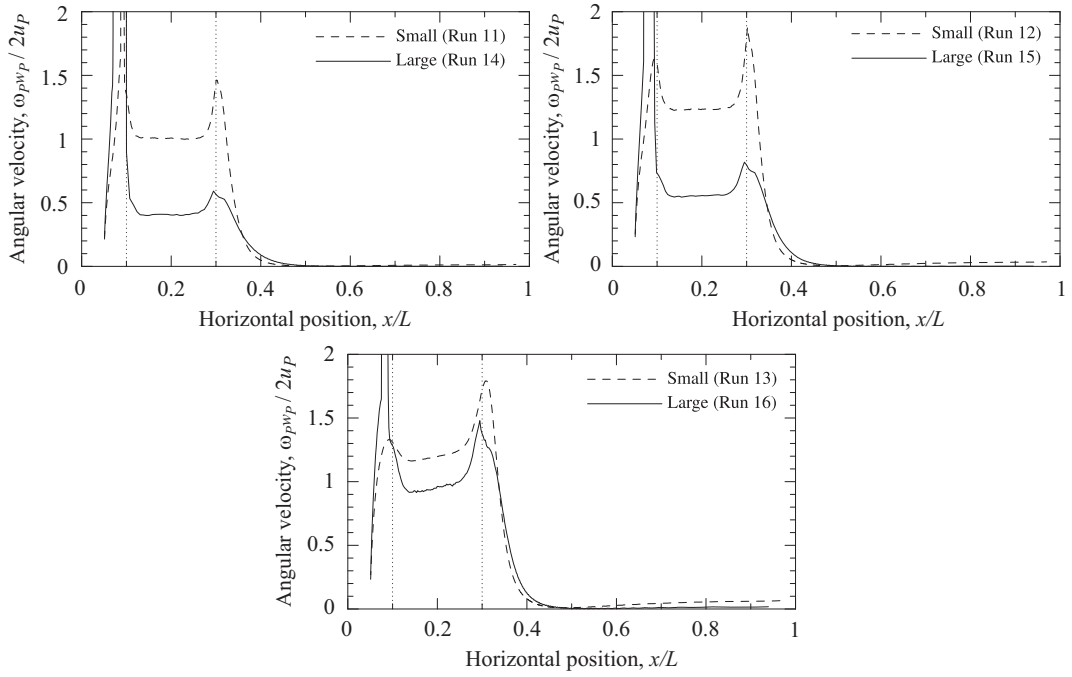

Fig. 11. Angular velocity of the sphere for the runs with varying pinch segment width. The vertical lines indicate the start and end of the pinched segment.

Author's personal copy

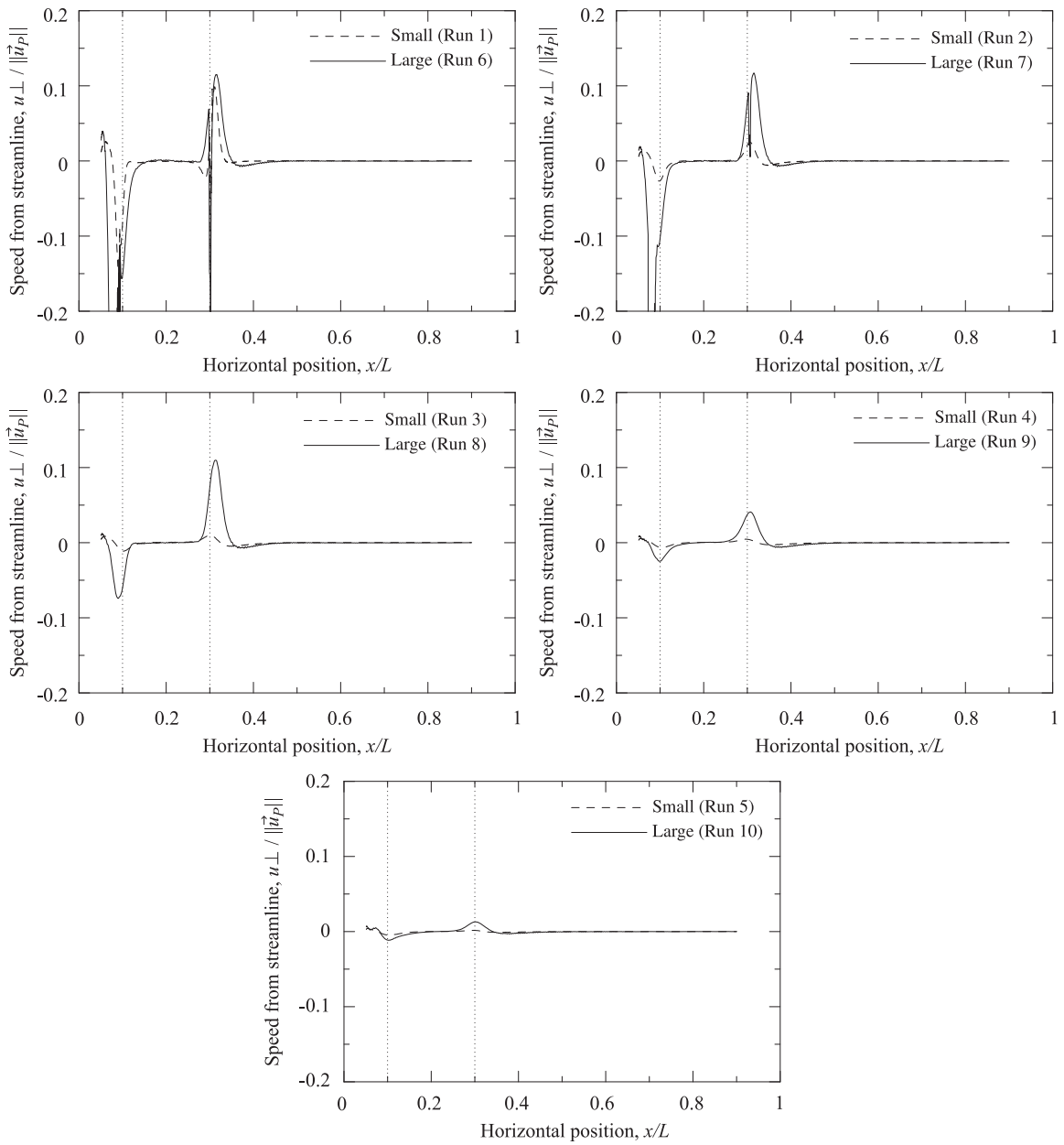

Fig. 12. Velocity perpendicular to streamline for the runs with varying flow ratios. The vertical lines indicate the start and end of the pinched segment.

At low diluent flow rates, small particles would pass nearly along the middle of the pinched segment, while the large particles could be attracted to the upper wall due to their larger size, causing upward deviation from the streamline.

Under the assumption that the particle does not disturb the flow, the Saffman lift force due to shear and the Magnus lift force due to rotation were estimated at the positions of the particles as they travelled through and exited the pinched segment. The correlation by Mei (1992) was used for the Saffman force, and the correlation by Oesterlé and Dinh (1998) was used for the Magnus force. It was found that the Saffman force would repel the particle from the wall while the Magnus force would attract the particle. The Saffman force was approximately two orders of magnitude higher than the Magnus force, indicating that the net force would cause repulsion from the wall. This discrepancy with the simulations can be explained by the possibility that the spheres disturb the flow significantly. Other lift and drag force models were considered. However, the available models deal with translating and rotating particles near one wall in a quiescent fluid (Zeng et al., 2005) or a linear shear flow (Lee and Balachandar, 2010; Lee et al., 2011a; McLaughlin, 1993; Zeng et al., 2009) and are not applicable to the PFF simulations in which four walls surround the particles and the shear flow is not linear. Di Carlo et al. (2009) note that the particle disturbs the flow field as the diameter of the sphere approaches the width of the channel. The large particles are likely sufficiently large relative to the size of channel that the deviation observed by Di Carlo et al. is relevant to the PFF simulations. The direction of the lift force observed in the PFF simulations may therefore be plausible given the complexity of the flow around a sphere translating and rotating in a narrow channel. Higher resolution simulations of the flow of a sphere in a microchannel could be used to further assess the validity of the simulation results.

Author's personal copy

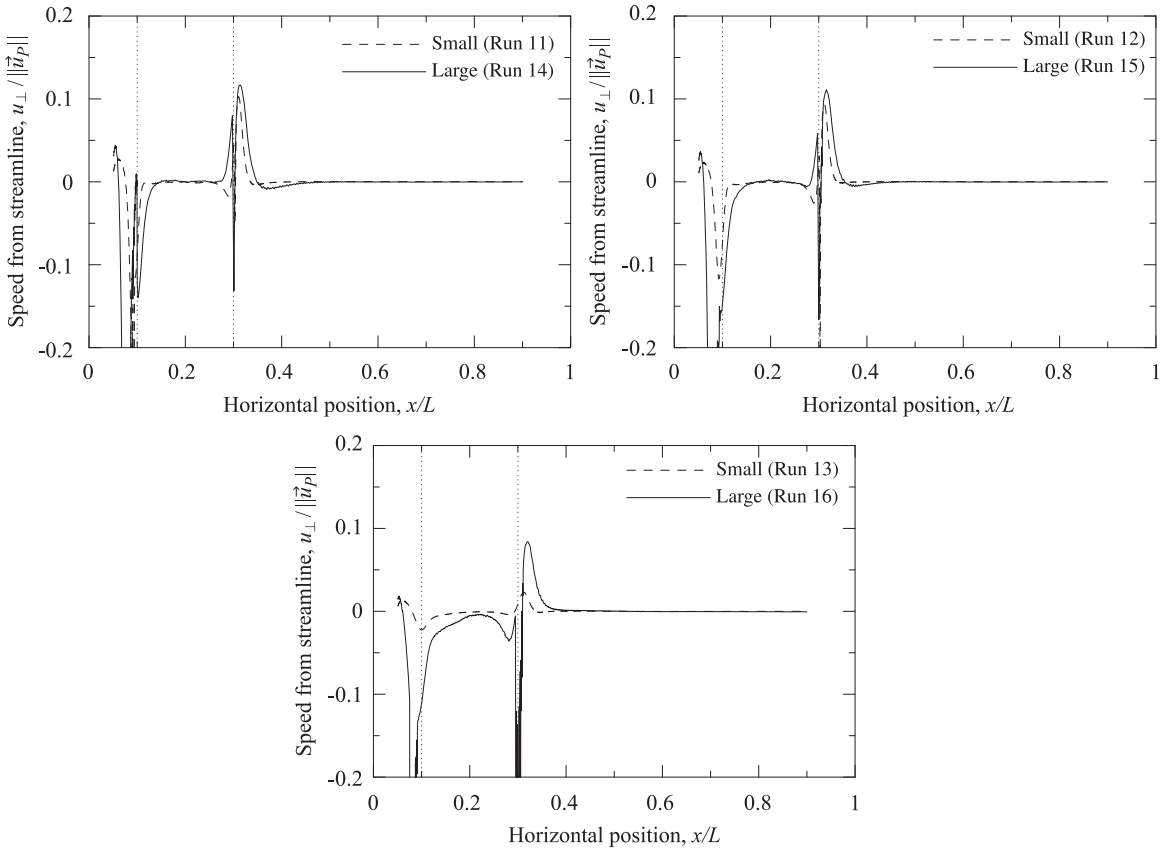

Fig. 13. Velocity perpendicular to streamline for the runs with varying pinch segment width. The vertical lines indicate the start and end of the pinched segment.

Fig. 14. Pressure field around the particle as it rotates and translates through the pinched segment during Run 7.

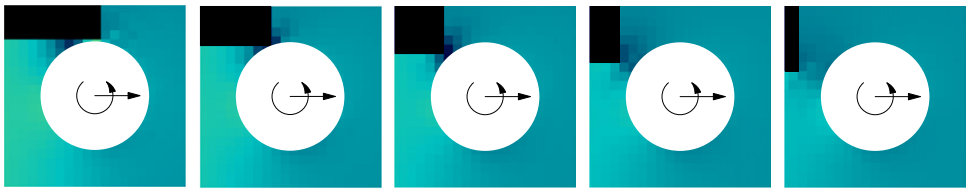

Fig. 15. Pressure field around the particle as it leaves the pinched segment during Run 7. Colour range is the same as in Fig. 14. The interval between each image is 500 time steps (0.36 ms). (For interpretation of the references to color in this figure legend, the reader is referred to the web version of this article.)

Author's personal copy

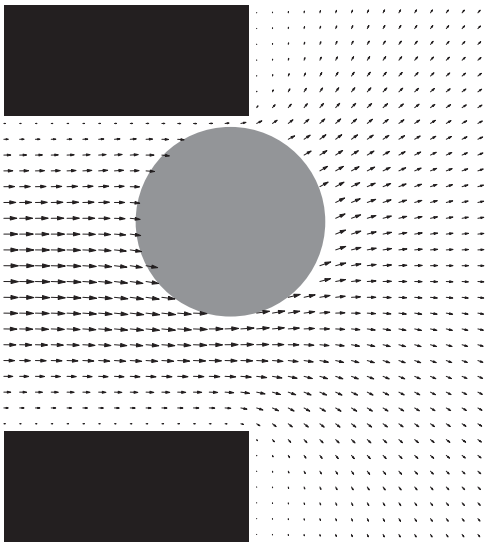

Fig. 16. Sample velocity field around the large particle as it exits the pinched segment in Run 7 after 35,000 time steps.

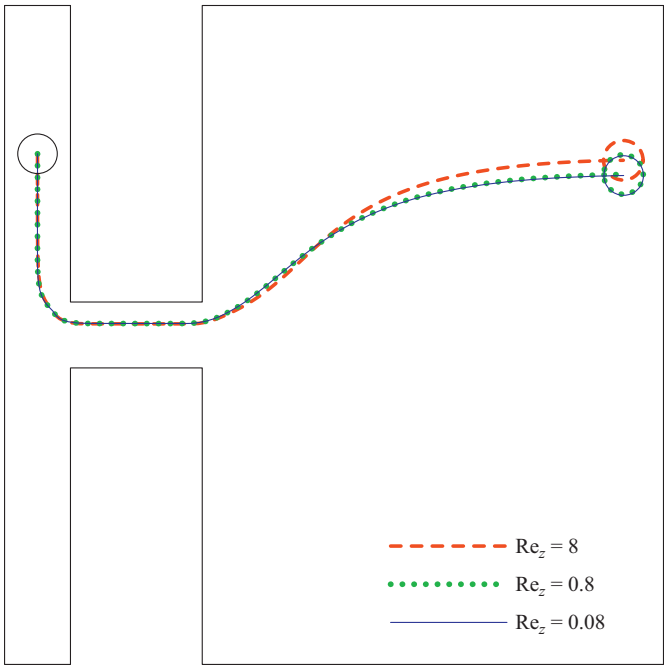

Fig. 17. Effect of the Reynolds number on the trajectory of a sphere through a PFF device.

3.6. *Effect of the Reynolds number*

We now consider the effect of the Reynolds number on the trajectory of the particles. While Yamada et al. (2004) chose a high-viscosity fluid (aqueous Dextran solution) to overcome experimental challenges, the simulations in the present work were scaled to match a less viscous fluid (water) due to stability and computational time constraints. To assess the significance of the different Reynolds numbers, two additional simulations were performed for the larger sphere size. In one simulation, the parameters were the same as in Run 7, but the Reynolds number was lowered by reducing the maximum fluid velocity from 0.01 to 0.001 l.u., resulting in a 10 times longer computational time. In the second simulation, the Reynolds number was raised by a factor of 10 by lowering the viscosity from 0.1143 to 0.01143 l.u. The surface points were not recalibrated for this lower viscosity; the impact of a different hydrodynamic radius is expected to be small. Fig. 17 shows the trajectories of the particles at the base case (Run 7) Reynolds number and the higher and lower Reynolds numbers. It can be seen that the trajectories for the base case and lower Reynolds number are nearly identical, indicating that comparison of the previous simulations with the lower Reynolds number experimental results is reasonable. The absence of significant difference suggests that up to Reynolds numbers around 1, the flow is determined by viscous stresses. The minimal change in the trajectories is consistent with the experimental evidence of Yamada et al. For flow rates ranging from 70 to 560 μl/h, corresponding to Re_z from 0.01 to 0.1, Yamada et al. observed a small change in the outlet positions of the particles. The simulation results suggest that this Reynolds number independence extends to $Re_z \approx 1$. The simulation at the highest Reynolds number shows significant deviation from the other two, demonstrating the effect of increasing inertia: the particle rises later in the wider segment and ends higher.

4. Conclusions

Direct simulations of pinched flow fractionation were performed using the lattice Boltzmann method. A system that was feasible to simulate was obtained by the use of parallelization and careful selection of geometric and fluid parameters. The final positions of large and small diameter spheres in the simulations were compared with the experimental work by Yamada et al. (2004). Since previous PFF modelling has relied on the assumption that particles follow the streamlines of the particle-free flow, the trajectories of the particles in the simulations were compared with these streamlines. Reasons for the deviation from the streamlines were examined, and the key role of lift forces related to particle–wall interactions was identified.

The trends in particle position due to changes in particle solution and diluent flow rate agreed qualitatively with experimental trends. Good agreement was also observed for the effect of the pinched segment width on separation performance. Since the simulations were performed at an order of magnitude higher Reynolds number than the experiments, additional simulations at ten times higher and lower Reynolds numbers were used to assess the impact of the difference in the Reynolds number. These simulations showed a minimal change in the large particle trajectory at the lower (near experimental) Reynolds number and a significant upward displacement of the large particle at the higher Reynolds number ($100 \times$ experimental).

Particles that were far from channel walls followed the streamlines of the undisturbed flow. This occurred when the diluent flow rate was sufficiently low or the pinched segment was sufficiently wide compared to the diameter of the particle. The simulated spheres rotate while in the pinch, as observed in experimental work on particles in confined flows (Di Carlo et al., 2009). Particles appear to deviate from the streamlines of the particle-free flow due to attraction to the walls caused by the formation of a low pressure region between the particle and the channel wall as it exits the pinched segment. This attraction causes large particles to move to streamlines that end higher in the outlet. The wall effect may explain why a sharp expansion is better than a gradual expansion, as observed by Yamada et al.: a particle would be attracted to the wall longer with a gradual expansion. Attraction to the upper wall may also explain why large particles reached a higher position in the outlet than the small particles, the reverse of the usual order, at low simulated diluent flow rates.

Author's personal copy

Future work will take a closer look at direct and hydrodynamic particle–wall interactions. The effect of wall and sphere roughness during particle–wall collisions on particle rotation and (related) lift forces will be assessed. Enhancing the resolution of the simulations and/or adding analytical (lubrication force) results for hydrodynamic interactions between a sphere and a wall may shed more light on why spheres deviate from streamlines. Other avenues for future research are simulations of PFF devices involving dense suspensions with multiple spheres passing through the device at the same time and simulations involving non-spherical and possibly deformable particles. It is anticipated that interactions between the particles of a suspension and the motion of non-spherical particles into and out of the pinched segment will have an important impact on separation performance.

Acknowledgements

O.S. gratefully acknowledges helpful discussions with Alexandr Kuzmin and Nitesh Goyal. This research has been enabled by the use of computing resources provided by WestGrid and Compute/Calcul Canada.

Appendix A. Verification of outlet boundary condition

A two-dimensional benchmark was used to assess the performance of the outlet boundary condition. This simulation had a width w in the y-direction of 21 nodes and a length L in the x-direction of 101 nodes. The kinematic viscosity was 0.1. A parabolic profile with a peak velocity (u_{max}) of 0.01 was imposed at the inlet ($x=0$). The mass conserving outlet condition was used at the right boundary ($x=L$). These parameters correspond to a channel Reynolds number of $Re_w = u_{max}w/\nu = 2.1$. The simulation was run for 20,000 time steps at which time a steady solution had been reached. The resulting velocity profile was compared with the analytical parabolic solution; excellent agreement was obtained. The pressure gradient in the y-direction was minimal, and the x-direction pressure gradient was within 0.2% of the theoretical prediction for planar Poiseuille flow. Thus, the proposed mass-conserving outlet condition provides accurate results when used with a laminar flow inlet condition, as required for the PFF simulations.

References

Aidun, C.K., Clausen, J.R., 2010. Lattice-Boltzmann method for complex flows. Annu. Rev. Fluid Mech. 42 (1), 439–472.
Akashi, N., Kushibiki, J.-I., Dunn, F., 2000. Measurements of acoustic properties of aqueous dextran solutions in the VHF/UHF range. Ultrasonics 38 (9), 915–919.
Andersen, K.B., Levinsen, S., Svendsen, W.E., Okkels, F., 2009. A generalized theoretical model for continuous particle separation in a microchannel having asymmetrically arranged multiple branches. Lab Chip 9 (11), 1638–1639.
Berger, S., Talbot, L., Yao, L.-S., 1983. Flow in curved pipes. Annu. Rev. Fluid Mech. 15, 461–512.
Chen, S., Doolen, G., 1998. Lattice Boltzmann method for fluid flows. Annu. Rev. Fluid Mech. 30, 329–364.
COMSOL AB, 2010. COMSOL Multiphysics Version 4.0a.
Derksen, J.J., 2009. Scalar mixing with fixed and fluidized particles in microreactors. Chem. Eng. Res. Des. 87 (4), 550–556.
Derksen, J.J., Larsen, R.A., 2011. Drag and lift forces on random assemblies of wall-attached spheres in low-Reynolds-number shear flow. J. Fluid Mech. 673, 548–573.
Derksen, J.J., Sundaresan, S., 2007. Direct numerical simulations of dense suspensions: wave instabilities in liquid-fluidized beds. J. Fluid Mech. 587, 303–336.
Di Carlo, D., Edd, J.F., Humphry, K.J., Stone, H.A., Toner, M., 2009. Particle segregation and dynamics in confined flows. Phys. Rev. Lett. 102 (9). 094503.
Eggels, J.G.M., Somers, J.A., 1995. Numerical simulation of free convective flow using the lattice-Boltzmann scheme. Int. J. Heat Fluid Flow 16 (5), 357–364.
Goldstein, D., Handler, R., Sirovich, L., 1993. Modeling a no-slip flow boundary with an external force field. J. Comput. Phys. 105, 354–366.
Jain, A., Posner, J.D., 2008. Particle dispersion and separation resolution of pinched flow fractionation. Anal. Chem. 80 (5), 1641–1648.
Ladd, A., 1994. Numerical simulations of particulate suspensions via a discretized Boltzmann equation. Part 2: numerical results. J. Fluid Mech. 271, 311–339.
Lee, H., Balachandar, S., 2010. Drag and lift forces on a spherical particle moving on a wall in a shear flow at finite Re. J. Fluid Mech. 657, 89–125.
Lee, H., Ha, M.Y., Balachandar, S., 2011a. Rolling/sliding of a particle on a flat wall in a linear shear flow at finite Re. Int. J. Multiphase Flow 37 (2), 108–124.
Lee, K.H., Kim, S.B., Lee, K.S., Sung, H.J., 2011b. Enhancement by optical force of separation in pinched flow fractionation. Lab Chip 11 (2), 354–357.
Maenaka, H., Yamada, M., Yasuda, M., Seki, M., 2008. Continuous and size-dependent sorting of emulsion droplets using hydrodynamics in pinched microchannels. Langmuir 24 (8), 4405–4410.
McLaughlin, J.B., 1993. The lift on a small sphere in wall-bounded linear shear flows. J. Fluid Mech. 246, 249–265.
Mei, R., 1992. An approximate expression for the shear lift force on a spherical particle at finite Reynolds number. Int. J. Multiphase Flow 18 (1), 145–147.
Mortensen, N.A., 2007. Comment on "pinched flow fractionation: continuous size separation of particles utilizing a laminar flow profile in a pinched microchannel". Anal. Chem. 79 (23), 9240–9241.
Oesterlé, B., Dinh, T.B., 1998. Experiments on the lift of a spinning sphere in a range of intermediate Reynolds numbers. Exp. Fluids 25 (1), 16–22.
Sangani, A., Acrivos, A., 1982. Slow flow through a periodic array of spheres. Int. J. Multiphase Flow 8 (4), 343–360.
Shardt, O., Derksen, J., 2011. Direct simulation of dense suspensions of non-spherical particles. In: ASME-JSME-KSME Joint Fluids Engineering Conference.
Somers, J.A., 1993. Direct simulation of fluid flow with cellular automata and the lattice-Boltzmann equation. Appl. Sci. Res. 51 (1), 127–133.
Takagi, J., Yamada, M., Yasuda, M., Seki, M., 2005. Continuous particle separation in a microchannel having asymmetrically arranged multiple branches. Lab Chip 5 (7), 778–784.
ten Cate, A., 2002. Turbulence and Particle Dynamics in Dense Crystal Structures. Ph.D. Thesis, Delft University of Technology.
van der Graaf, S., Nisisako, T., Schroën, C.G.P.H., van der Sman, R.G.M., Boom, R.M., 2006. Lattice Boltzmann simulations of droplet formation in a T-shaped microchannel. Langmuir 22 (9), 4144–4152.
Vig, A.L., 2010. Pinched Flow Fractionation – Technology and Application. Ph.D. Thesis, Department of Micro- and Nanotechnology Technical University of Denmark.
Vig, A.L., Kristensen, A., 2008. Separation enhancement in pinched flow fractionation. Appl. Phys. Lett. 93 (20), 203507.
Yamada, M., Nakashima, M., Seki, M., 2004. Pinched flow fractionation: continuous size separation of particles utilizing a laminar flow profile in a pinched microchannel. Anal. Chem. 76 (18), 5465–5471.
Zeng, L., Balachandar, S., Fischer, P., 2005. Wall-induced forces on a rigid sphere at finite Reynolds number. J. Fluid Mech. 536, 1–25.
Zeng, L., Najjar, F., Balachandar, S., Fischer, P., 2009. Forces on a finite-sized particle located close to a wall in a linear shear flow. Phys. Fluids 21 (3), 033302.